Displaced Drude peak from π-ton vertex corrections

J. Krsnik [1,2,*] O. Simard [3,4,5] P. Werner [4] A. Kauch [1] and K. Held [1]

[1]*Institute of Solid State Physics, TU Wien, 1040 Vienna, Austria*
[2]*Department for Research of Materials under Extreme Conditions, Institute of Physics, HR-10000 Zagreb, Croatia*
[3]*CPHT, CNRS, Ecole Polytechnique, Institut Polytechnique de Paris, 91128 Palaiseau, France*
[4]*Department of Physics, University of Fribourg, 1700 Fribourg, Switzerland*
[5]*Department of Physics, Collège de France, Université PSL, 75005 Paris, France*

Correlated electron systems often show strong bosonic fluctuations, e.g., of antiferromagnetic nature, around a large wave vector such as $\mathbf{q} = (\pi, \pi \ldots)$. These fluctuations can give rise to vertex corrections to the optical conductivity through the (transversal) particle-hole channel, coined π-ton contributions. Previous numerical results differed qualitatively on how such vertex corrections alter the optical conductivity. Here we clarify that π-ton vertex corrections lead to a displaced Drude peak, by studying the weakly correlated regime of a one-dimensional single-orbital Hubbard model. The proximity and enhancement of the effect when approaching a phase transition of, e.g., antiferromagnetic nature can be utilized for discriminating π-tons in experiments from other physics leading to a displaced Drude peak.

I. INTRODUCTION

Optical probes are important tools in condensed-matter physics for studying the electronic properties of materials. The response of an electrical current to an external dynamic electric field is described by the optical conductivity. For a generic metallic system, it is peaked at zero frequency as predicted in the classical Drude theory [1,2], while for semiconducting or insulating systems an optical gap in its spectrum appears, since a nonzero photon energy is needed to excite electrons across the band gap. In the simplest theory, both of these spectra can be described by the uncorrelated propagation of an electron and a hole, corresponding in the diagrammatic language to the bubble term. In certain cases, however, correlations between the excited electron and hole lead to novel physical phenomena, requiring a proper treatment of vertex correction contributions. The prime examples are excitons in semiconductors [3,4] and weak localization in disordered systems [5–8]. In the former case, the electron and hole form a bound state giving rise to excitonic peaks in the optical gap, while the suppression of the dc conductivity due to the destructive interference of the electron wave function occurs in the latter case.

Naturally, the question arises: Do vertex corrections play an equally important role in shaping an optical conductivity spectrum of correlated electron systems? This long-standing fundamental question has captured the interest of the community for several decades [9–21]. However, it was only until quite recently that a convenient classification and an identification of the important class of vertex corrections in correlated electron systems was carried out [22–24]. This was

possible due to the recent methodological advances in using the parquet equations [25–27] within the dynamical vertex approximation [28–30] and the parquet approximation [25]. This allows for classifying and studying the vertex corrections according to the two-particle reducibility. As a result, it was found that the dominant vertex corrections in prototypical models of strongly correlated electrons are those in the transversal particle-hole ($\overline{ph}$) channel. This is because the $\overline{ph}$ channel can pick up bosonic fluctuations at an arbitrary wave vector, even though the transfer momentum of the photon is zero. Specifically, strong antiferromagnetic (AFM) or charge density wave fluctuations at $\mathbf{k} - \mathbf{k}' \approx (\pi, \pi, \ldots)$ enter the optical conductivity via the $\overline{ph}$ channel, and have been coined π-ton vertex corrections [23]. Excitons, on the other hand, emerge from the particle-hole (ph) channel, and weak localization corrections from the particle-particle (pp) channel.

In Refs. [22–24], π-ton vertex corrections were studied for several correlated models both in the insulating and in the metallic phases. In the insulating cases, they were reported to shift the optical gap, while in the metallic phases, a renormalization of the Drude peak was observed, but also the displaced Drude peak profile of the total optical conductivity in the case of the metallic phase of the Falicov-Kimball model [31]. Soon after these numerical studies, simplified random phase approximation (RPA) calculations of the π-ton vertex corrections were performed [32–34], with the aim of studying in more detail their characteristics in the weakly correlated regime of the Hubbard model. While in Ref. [34] only a temperature dependent sharpening and broadening of the Drude peak was reported, in Refs. [32,33] it was argued that an additional π-ton peak may arise next to an existing Drude peak. Such striking differences could have originated from several sources, such as the dimensionality of a system, i.e., one-dimensional (1D) in Refs. [32,33] and two-dimensional

*Contact author: juraj.krsnik@tuwien.ac.at

(2D) in Ref. [34], Hubbard bands present in Refs. [32,33], but not in Ref. [34], or perhaps the pitfalls of the analytic continuation of the optical spectra to real frequencies [32].

In this paper, we reconcile the previously conflicting results by evaluating the π-ton vertex corrections in a weakly correlated regime of a single-orbital Hubbard model within the RPA using two different approaches. Our main finding is that irrespective of dimensionality, the presence of Hubbard bands, and the use of an analytic continuation, both approaches agree on the qualitative frequency dependence of the π-ton vertex corrections, which may yield the displaced Drude peak in the total optical conductivity.

A displaced Drude peak is not an uncommon phenomenon and has been experimentally observed for decades [35–57]. As already mentioned, it naturally arises as a consequence of the weak localization effects in disordered systems. However, its unambiguous presence in correlated materials calls for a better or alternative understanding of the phenomenon, with several theories already put forth [58–61]. While in Ref. [58] it is explained in terms of the hydrodynamics of short-range quantum critical fluctuations of incommensurate density wave order, it is argued that quantum localization corrections may also arise due to the slow phononic fluctuations [59,60] or charge fluctuations mediated by long-range Coulomb interaction coexisting with lattice frustration [61]. Here we show that the strong AFM fluctuations through the π-ton vertex corrections may as well lead to the displaced Drude peak. This represents a microscopic theory of the displaced Drude peak formation in a clean prototypical correlated electron system, where the bosonic fluctuation emerges from intrinsic many-body electron interactions.

The outline of the paper is as follows: In Sec. II, we briefly introduce the Hubbard model and how optical conductivities are calculated. Further details are given for the three different parameter sets studied in Sec. II A, and the RPA calculation of vertex corrections in Sec. II B. Section III presents our results. Here, in Sec. III A, we demonstrate the occurrence of a displaced Drude peak; in Sec. III B we employ an adaptive ν- and **k**-space integration and show results in the immediate vicinity of the antiferromagnetic phase transition; and in Sec. III C we show the temperature dependence of the peak position and height of the displaced Drude peak. Finally, in Sec. III D, we discuss why previous calculations did not see the displaced Drude peak, before summarizing our results in Sec. IV.

II. MODEL AND METHODS

We consider a single-orbital Hubbard model on a D-dimensional hypercubic lattice

$$\hat{\mathcal{H}} = -t \sum_{\langle ij \rangle \sigma} \hat{c}^{\dagger}_{i\sigma} \hat{c}_{j\sigma} + U \sum_{i} \hat{n}_{i\uparrow} \hat{n}_{i\downarrow}, \qquad (1)$$

where $\hat{c}^{\dagger}_{i\sigma}$ ($\hat{c}_{i\sigma}$) denotes the fermionic creation (annihilation) operator for an electron at lattice site i with spin σ, and $\hat{n}_{i\sigma} = \hat{c}^{\dagger}_{i\sigma} \hat{c}_{i\sigma}$ is a number operator. We take into account hoppings only between nearest neighbors, indicated by $\langle ij \rangle$ in the sum over lattice sites (each pair of neighboring sites is counted once in the sum). In all our calculations, we set hopping $t \equiv 1$ as the unit of energy, as well as $\hbar \equiv 1$, $k_B \equiv 1$, electric charge
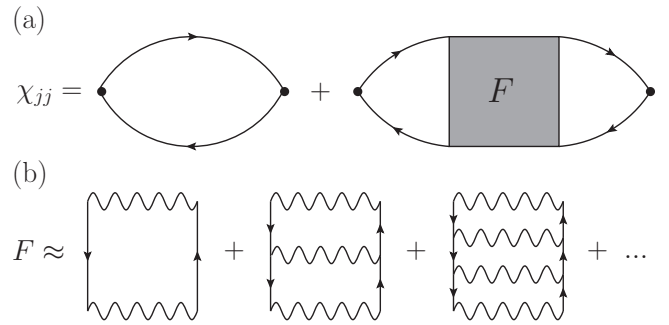
FIG. 1. (a) Diagrammatic representation of the current-current correlation function χ_{jj} with bubble (left) and vertex contribution (right). (b) Diagrammatic representation of the π-ton vertex corrections in the $\overline{ph}$ channel within the RPA. Here, the solid lines represent the fermion Green's functions G, the wavy lines the Hubbard interaction U, F is the vertex function, while light-fermion vertices are denoted by solid circles.

$e \equiv 1$, and lattice constant $a \equiv 1$. We keep the value of the local interaction $U \leqslant 2$ and hence focus on the weakly correlated metallic state. Finally, we consider the half-filled case for which we anticipate the presence of strong antiferromagnetic fluctuations.

We are interested in calculating the optical conductivity $\sigma(\omega)$ for the model Hamiltonian Eq. (1). We obtain it from the current-current correlation function χ_{jj}, which we calculate in turn using two distinct approaches. Within the first approach, here called the real-axis approach, the current-current correlation function $\chi_{jj}(\omega)$ is calculated directly on the real-frequency axis using the formulas derived in Ref. [34], see Appendix A for the final expressions, Eqs. (A2)–(A6). The optical conductivity is then simply obtained as $\sigma(\omega) = \text{Im}\chi_{jj}(\omega)/\omega$, while its static limit, that is the dc conductivity, $\sigma_{\text{dc}} = \lim_{\omega \to 0} \sigma(\omega)$, is handled by extrapolating finite frequency values to the zero frequency limit. In the second approach, here referred to as the imaginary-axis approach, the current-current correlation function $\chi_{jj}(i\omega_n)$ is instead calculated on the imaginary-frequency axis as described in Ref. [32] and briefly summarized in Appendix A. To get the real frequency optical conductivity spectrum, the use of analytic continuation is thus needed, which we perform using the `ana_cont` package [62]. Common to both approaches is that χ and σ are separated into the bubble (BUB) and the vertex (VERT) contribution, Fig. 1(a). For the bubble contribution, only the knowledge of the fermion Green's functions G is needed, while for the vertex contribution, the vertex function F is additionally required. In the following, we outline the ideas behind modeling both G and F, such that π-ton vertex corrections are treated within the RPA.

A. Models for the self-energy

The aforementioned real-axis approach allows for any fermion Green's function G, as long as the self-energy Σ, with or without momentum dependence, is known on the real-frequency axis. Since neglecting the momentum and retaining only the frequency dependence of the self-energy in the spirit of dynamical mean-field theory (DMFT) [63] is

sufficient to capture the effects of Hubbard bands on the π-ton vertex corrections, we do not consider the effects of a possible momentum dependence of Σ in the following. In particular, in order to address the influence of Hubbard bands as well as dimensionality effects on the π-ton vertex corrections, we define three sets of parameters S_{DMFT}, S_{1D}, and S_{2D} to model the fermion Green's functions as follows.

1. Parameter set S_{DMFT}

In the spirit of Ref. [33], the parameter set S_{DMFT} regards a 1D lattice with $U = 2$, and the DMFT self-energy obtained with iterated perturbation theory (IPT) [64]. Such a choice of self-energy is convenient for the calculation of the current-current correlation function within the imaginary-axis approach [32]. Of the several temperatures considered in Ref. [33], we mainly focus on the case $\beta = 12.5$. For the corresponding temperature $T = \beta^{-1}$, it has been reported that the π-ton vertex corrections show a distinct broad peak at $\omega \approx 0.35$ [33]. We note that the DMFT phase diagram in 1D resembles that of higher dimensional systems and does not capture the presence of a Mott gap for any $U > 0$, however small, at half-filling. Only for U of the order of the bandwidth does a Mott gap open. Hence, our 1D results should primarily serve as a proxy for the behavior of the π-ton vertex corrections in higher dimensional systems or slightly away from the half-filled case.

2. Parameter set S_{1D}

Motivated by studying the effects of Hubbard bands on the π-ton vertex corrections, we introduce the second parameter set S_{1D}, referring again to the 1D lattice with $U = 2$, but now with the simplified frequency independent self-energy,

$$\Sigma = -i\Delta(T), \quad \Delta(T) = 0.1547 + 1.637\, T^2. \quad (2)$$

This form of self-energy can be rationalized by the ever-present impurity scattering and resembles the Fermi-liquid-like temperature behavior [65]. The choice of parameter values entering $\Delta(T)$ is motivated in Ref. [34].

The difference between S_{DMFT} and S_{1D} is that the former involves both the quasiparticle and Hubbard bands, while the parameter set S_{1D} involves only the former. By comparing the optical conductivity between both sets, we can thus single out features that result from the presence of Hubbard bands.

3. Parameter set S_{2D}

Our third set of parameters S_{2D} relates to the 2D square lattice with $U = 1.9$ and the same self-energy as in Eq. (2). The point of introducing it is to study differences between the π-ton vertex corrections in 1D and 2D cases. For both parameter sets S_{1D} and S_{2D}, we calculate the current-current correlation function using the real-axis approach.

B. Vertex function

The evaluation of the vertex contribution to the current-current correlation function requires the knowledge of the full density component of the two-particle vertex $F_d^{kk'q}$ [26,66]. Following arguments in Ref. [23], we, however, only focus on the vertex contributions $F_{d,\overline{ph}}^{kk'q}$ coming from the $\overline{ph}$ channel:

π-ton vertex corrections, which are supposed to be dominant in the Hubbard model. In order to be able to evaluate the corresponding π-ton vertex contributions to the current-current correlation function within the real-axis approach of Ref. [34] and/or imaginary-axis approach of Ref. [32], we further assume that the vertex function depends only on one transfer momentum and energy, $F_{d,\overline{ph}}^{kk'q} \equiv F_{d,\overline{ph}}^{k-k'}$. Here $k = (\mathbf{k}, \nu)$ denotes a combined momentum and frequency index. Generally, such contributions may still be quite complicated, but diagrammatically they can be represented as vertical ladders in terms of the irreducible vertex $\Gamma_{\overline{ph}}$. Following further the modeling approach of the vertex function described in Refs. [32,34], we focus on the $\uparrow\uparrow\downarrow\downarrow \equiv \uparrow\downarrow$ spin component and take for the irreducible vertex $\Gamma_{\overline{ph}} = -U$. Namely, the building blocks of our vertical ladders are the interaction U and the Lindhard function $\chi^0_q = -\frac{1}{\beta}\sum_k G_k G_{k+q}$, see Fig. 1(b). This series of vertical ladders can be summed up to infinite order to finally yield the RPA version of the π-ton vertex function

$$F_{\overline{ph},k-k'}^{\text{RPA}} = \frac{U^2 \chi^0_{k-k'}}{1 - U\chi^0_{k-k'}} = U^2 \chi^{\text{RPA}}_{k-k'}, \quad (3)$$

where $\chi^{\text{RPA}}_{k-k'}$ is the RPA magnetic susceptibility, which we use in all our calculations of the vertex contribution to the current-current correlation function. Note that $F_{\overline{ph},k-k'}^{\text{RPA}}$ is fully determined by $G(\Sigma)$, U, and T.

Let us emphasize that vertex corrections to the optical conductivity from the crossing symmetrically related RPA ladder in the particle-hole channel, instead of the particle-hole transversal one in Eq. (3), exactly vanish for a local interaction. The same is true for a local vertex, which has the consequence that there are actually no vertex corrections in DMFT [67,68]. One has to go beyond DMFT for studying vertex contributions to the optical conductivity in one orbital models.

1. Paramagnetic-antiferromagnetic transition

For a given parameter set S_i, there exists a critical temperature $T_c = \beta_c^{-1}$ for which the vertex in Eq. (3) diverges. Within our model, this divergence signals the paramagnetic-to-antiferromagnetic phase transition. Due to the RPA treatment of the vertex, the transition appears at nonzero temperature even for 1D and 2D systems, violating the Mermin-Wagner theorem [69]. Hence, our results should again serve only as a proxy for the behavior of the π-ton vertex corrections near the transition boundary. Once the critical temperature is determined, we place ourselves within the paramagnetic metallic state with $T \geqslant T_c$. Then we lower the temperature towards the critical one, thereby enhancing the antiferromagnetic fluctuations and the overall effect of the π-ton vertex corrections.

There is no guarantee that the T_c, determined as the temperature at which the RPA vertex in Eq. (3) diverges, matches the Néel temperature T_N obtained by the IPT solver. Indeed, while the two values are quite close for $U \leqslant 1$ [32], for larger values of U the discrepancies between the two become larger. Therefore, a renormalized U_r was introduced in Ref. [32]

$$F_{\overline{ph},k-k'}^{\text{RPA},r} = \frac{U^2 \chi^0_{k-k'}}{1 - U_r \chi^0_{k-k'}}, \quad (4)$$
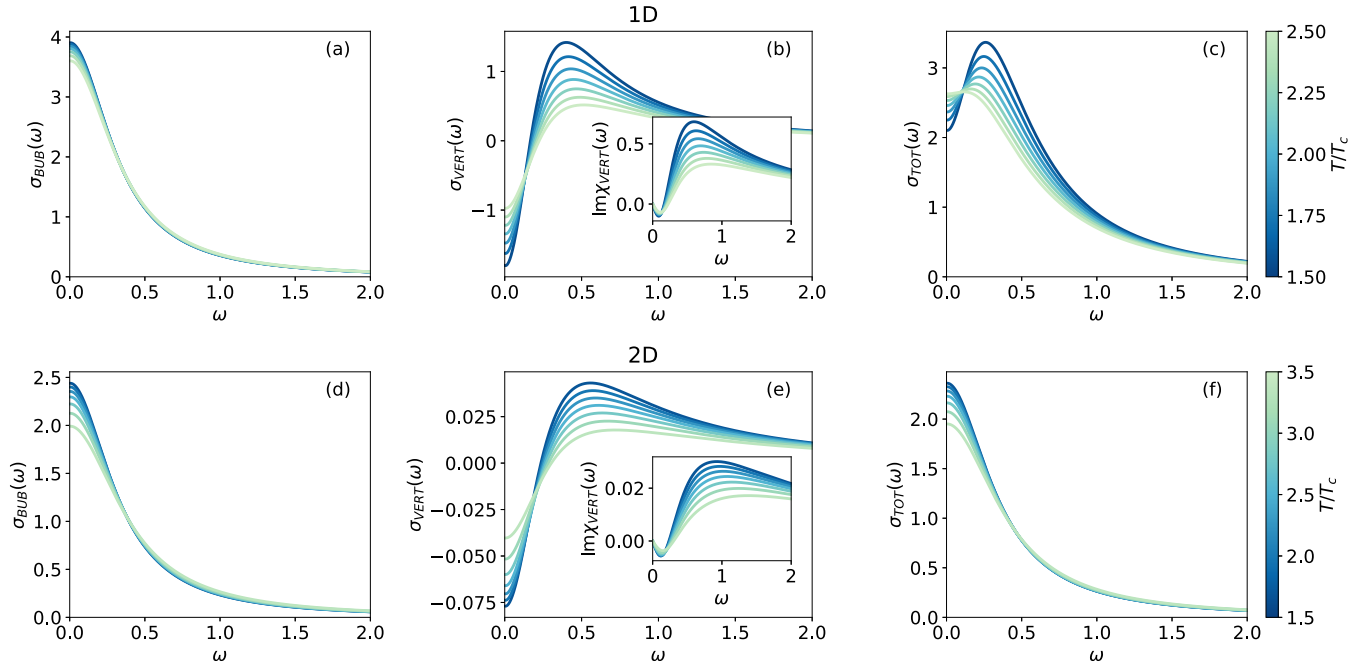
FIG. 2. Bubble [(a) and (d)], RPA π-ton vertex [(b) and (e)], and total contribution [(c) and (f)] to the optical conductivity for the parameter sets S_{1D} [(a)–(c)] and S_{2D} [(d)–(f)] and several temperatures T. The insets show the corresponding RPA π-ton vertex contributions to the current-current correlation function.

to push T_c towards T_N. For the parameter set S_{DMFT} this is achieved by taking $U_r = 1.33$, yielding $\beta_c \approx \beta_N \approx 20$ [33].

Regarding parameter sets S_{1D} and S_{2D}, we keep $U_r = U$, resulting in $\beta_c \approx 23$ and $\beta_c \approx 19$ for the former and the latter parameter set, respectively. It now becomes apparent that all parameter sets are chosen such that their T_c (β_c) are roughly similar.

2. Ornstein-Zernike form of the vertex function

Close to the phase transition boundary, in the presence of strong antiferromagnetic fluctuations, the magnetic susceptibility and thus our π-ton vertex function can be well approximated by the Ornstein-Zernike correlation function of the form [70–72]

$$F_{\mathbf{q},\omega}^{OZ} = \frac{A}{\xi^{-2} + (\mathbf{q} - \mathbf{Q})^2 - i\lambda\omega}. \qquad (5)$$

Here ξ is the correlation length of the antiferromagnetic fluctuations, while A and λ represent their effective coupling strength to fermions and the damping rate, respectively. For our half-filled Hubbard model $\mathbf{Q} = (\pi, \pi, \dots)$. One of the advantages of working with the Orsntein-Zernike vertex function is that it can be readily calculated on the fly for any $\mathbf{q}$ and ω, which we exploit to adaptively integrate the vertex contribution to the current-current correlation function within the real-axis approach close to the transition boundary. For practical purposes, in all our actual calculations involving Eq. (5) for the vertex function, we use an empirically more robust formula with $(\mathbf{q} - \mathbf{Q})^2 \rightarrow 4 \sum_i \sin^2(\frac{q_i - Q_i}{2})$ [73].

III. RESULTS

A. Displaced Drude peak from π-ton vertex corrections

Optical conductivities calculated directly on the real-frequency axis using Eqs. (A2)–(A6) and the RPA vertex function in Eq. (3) for the parameter sets S_{1D} and S_{2D} are shown in Figs. 2(a)–2(c) and Figs. 2(d)–2(f), respectively. The corresponding summations over the Brillouin zone are performed on the grid sizes $N_k = 200$ and $N_k = 40 \times 40$ for the 1D and 2D cases, respectively. The remaining integrals over frequencies are evaluated using the trapezoidal rule on the grids with $N_\nu = 3193$ points in the range $[-8, 8]$ in 1D and on the grids with $N_\nu = 1593$ points in the range $[-7.6, 7.6]$ in the 2D cases. These choices of summation/integration grids were thoroughly checked to produce converged results for all the temperatures considered in Fig. 2. For lower temperatures approaching the critical temperature T_c, the convergence of the π-ton vertex contribution becomes numerically more and more demanding. We discuss this issue in more detail in the next Sec. III B.

As expected, the bubble contribution to the optical conductivity σ_{BUB}, shown in Figs. 2(a) and 2(d), gives the Drude peak in both 1D and 2D cases. The corresponding widths and maxima of these peaks are governed by the fermion scattering rate, which is, with our choice of parameter sets S_{1D} and S_{2D}, given simply by $\tau(T) = \frac{1}{2\Delta(T)}$. Correspondingly, the magnitudes of σ_{BUB} in both Figs. 2(a) and 2(d) are roughly similar.

On the other hand, while the π-ton vertex contributions to the optical conductivity, σ_{VERT} in Figs. 2(b) and 2(e), show qualitatively similar behavior in both cases (1D and 2D), their magnitude is up to two orders of magnitude larger in the former case, at least for the considered temperature ranges. Taking that into account together with the peculiar

frequency dependence of the π-ton vertex contributions, the resulting total optical conductivity, $\sigma_{\text{TOT}} = \sigma_{\text{BUB}} + \sigma_{\text{VERT}}$, in Figs. 2(c) and 2(f) apparently exhibits quite different structures depending on the dimension. In particular, the results in Fig. 2 suggest that the π-ton vertex corrections suppress the optical conductivity at low frequencies and develop a broad maximum at some intermediate frequency, while for larger frequencies they asymptotically decay to zero. If the magnitude of such vertex corrections is large, as is the case in our 1D calculations, then the sum of the bubble and the π-ton vertex contributions results in a displaced Drude peak, as can be seen in Fig. 2(c). In contrast, if the magnitude of such vertex corrections is small compared to the bubble contribution, then the sum results in a renormalized Drude peak, as in our 2D calculations, see Fig. 2(f). Note that the smallness of π-ton vertex corrections and the absence of a π-ton peak in 2D was already reported in Ref. [34], with the caveat that in Ref. [34] a sign change of the π-ton vertex corrections in the dc limit occurred close to the transition. Here, we see that they do not change their qualitative behavior by lowering the temperature, at least in the regime for which convergence of Eqs. (A3)–(A6) can be achieved. Therefore, we see only a broadening of the Drude peak in Fig. 2(f). In the following, we get even closer to the phase transition boundary, enhancing thus AFM fluctuations and π-ton vertex contributions, and present further arguments in favor of the formation of the displaced Drude peak in the 1D case.

B. π-ton vertex corrections close to the transition boundary

Close to the paramagnetic-antiferromagnetic phase transition the π-ton vertex function resembles the Ornstein-Zernike form of Eq. (5). As the temperature is lowered towards the critical temperature, the correlation length ξ of the antiferromagnetic fluctuations increases, resulting in the confinement of the π-ton vertex function around momentum $\mathbf{Q} = (\pi, \pi, \dots)$ and frequency $\omega = 0$. To be specific, the widths of the Ornstein-Zernike function around these points read

$$\Gamma_q \sim \frac{1}{\xi}, \quad \Gamma_\omega \sim \frac{1}{\lambda \xi^2}, \tag{6}$$

which are getting narrower as the transition boundary is approached.

From the computational point of view, to resolve such fine momentum and frequency features of the π-ton vertex function we would need to use sufficiently dense grids, $\Gamma_q \gg N_k^{-1}$ and $\Gamma_\omega \gg N_\nu^{-1}$. This quickly becomes a numerical bottleneck if equidistant grids are used, especially in the 2D case, which involves four momentum and two frequency summations/integrations in Eqs. (A2)–(A6). For that reason, we focus on the parameter set S_{1D}, and adjust the multidimensional adaptive integration package `cubature` [74] to our needs, in order to evaluate the π-ton vertex contributions to the optical conductivity all the way down to the transition boundary.

Adaptive integration requires computing the integrand on the fly, which is inconvenient with the RPA π-ton vertex function since it involves momentum and frequency summations at each call. For this reason and since the Ornstein-Zernike
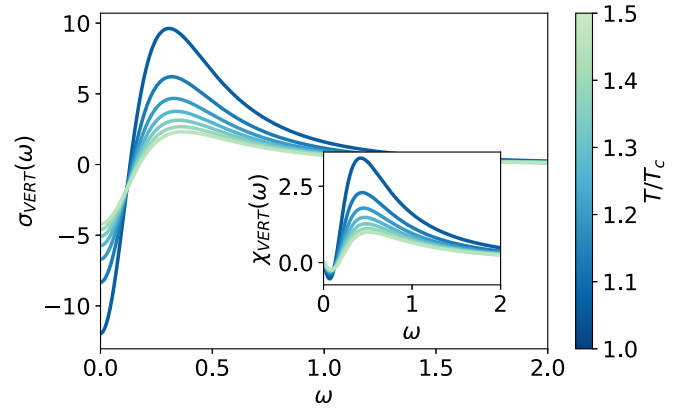
FIG. 3. π-ton vertex corrections to the optical conductivity and the current-current correlation function (inset) calculated with the Ornstein-Zernike vertex function and an adaptive integration for temperatures approaching the critical temperature, T_c, for the parameter set S_{1D}.

form close to the critical temperature approximates the π-ton vertex function well, we first calculate the RPA π-ton vertex function in Eq. (3) using dense momentum and frequency grids, and then fit it with the Ornstein-Zernike form in Eq. (5) to obtain A, ξ, and λ for a given temperature. In this way, we have the vertex function $F_{\mathbf{q},\omega}^{\text{OZ}}$ as a simple function that can be conveniently used for adaptive integration of the π-ton vertex corrections according to Ref. [34].

The temperature dependence of the Ornstein-Zernike parameters for the parameter set S_{1D} obtained by fitting Eq. (5) to the RPA π-ton vertex function is shown in Appendix B, while the corresponding π-ton vertex contributions to the optical conductivity obtained with the adaptive integration are shown in Fig. 3. More details on the fitting procedure can also be found in Appendix B. Evidently, the π-ton vertex contributions continue to show a similar qualitative trend as in the RPA case all the way down to the critical temperature. In particular, they do not change the sign in the dc limit close to the phase transition. Note also that the magnitude of the π-ton vertex corrections is larger with the OZ vertex function than with the RPA π-ton vertex function. Nevertheless, their magnitude keeps growing even larger as the transition boundary is approached due to the enhanced antiferromagnetic fluctuations, leading to an increasing suppression of the dc conductivity and an increasingly pronounced maximum at finite frequencies.

We note that at a certain point our approximations will fail and one would need to revisit them both from the point of view of the fermion Green's function, G, and the vertex function, F. It can be already inferred from Fig. 3 that the magnitude of the π-ton vertex contributions at low frequencies may exceed that of the bubble, leading to unphysical negative spectral weight in the total optical conductivity. The intention of the present paper is, however, to point out that the π-ton vertex corrections may lead to a displaced Drude peak, not to properly study all of their quantitative features. This requires more sophisticated calculations beyond RPA. In particular, fulfillment of Ward identities [75,76] can become important for quantitative predictions. To the best of our knowledge,
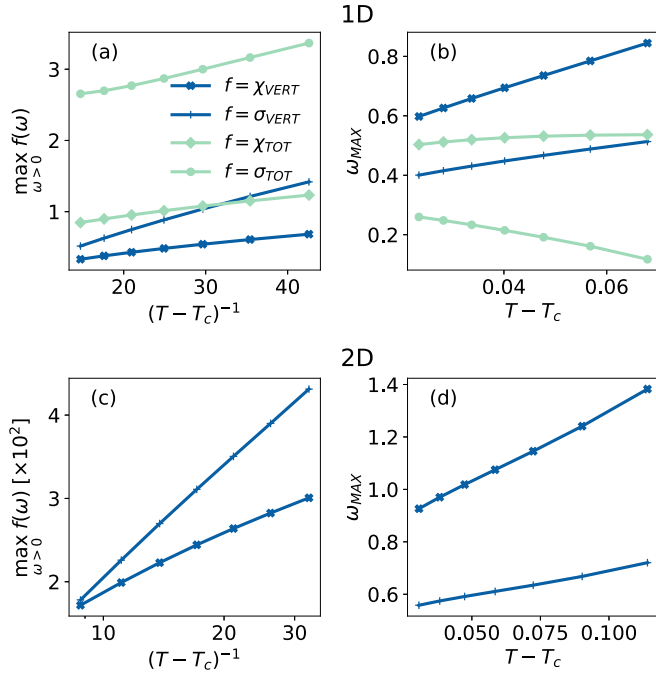
FIG. 4. [(a) and (c)] Temperature dependence of the maxima of the current-current correlation function ($f = \chi$) and the optical conductivity ($f = \sigma$) shown separately for the vertex (VERT; blue lines) and total contribution (TOT; green lines). [(b) and (d)] Frequencies ω_{MAX} associated with the maxima. The top panels (a) and (b) show the 1D S_{1D} and the bottom panels (c) and (d) the 2D S_{2D} results.

more sophisticated approximations or numerical approaches will likely not be feasible at the moment with the required accuracy, i.e., using dense ν- and $\mathbf{k}$-meshes, and eventually real frequencies.

In the 1D case, there are numerically accurate methods that are capable of calculating the full optical conductivity, e.g., the density matrix renormalization group (DMRG) [77–79]. DMRG results can in principle be decomposed into the bubble and vertex contribution, and the influence of vertex corrections and the contribution from π-ton diagrams (see Ref. [23] supplementary material Sec. E) could thus be studied.

C. Temperature dependence of the displaced Drude peak frequency and height

The displaced Drude peak has been experimentally observed in a great variety of compounds, ranging from cuprates, and transition metal oxides to organic conductors and Kagome metals [35–57]. The common feature in all of these experimental findings is that the displaced Drude peak position is an increasing function of temperature, $\omega_{\text{MAX}} \sim T^\alpha$, with the coefficient α falling in the range, $0 < \alpha < 3/2$ [59]. To compare our π-ton theory with this robust experimental feature, we show in Fig. 4 the temperature dependence of the position of the maxima in both the current-current correlation function and optical conductivity, as well as the temperature dependence of the maximum values themselves. For the parameter set S_{2D}, we focus only on the π-ton vertex contribution since the displaced Drude peak is not yet present in the total optical

conductivity, while for the parameter set S_{1D} we consider the total, bubble plus π-ton, contribution as well.

In both the 1D and 2D systems, the position of the maxima of the π-ton vertex contributions, χ_{VERT} and σ_{VERT} in Figs. 4(b) and 4(d), is clearly an increasing function of temperature, with a roughly linear dependence of the maximum position, $\omega_{\text{MAX}} \sim (T - T_c)$. In 1D, these vertex corrections lead to a clearly visible displaced Drude peak in the total optical conductivity, with its position rather decreasing with increasing temperature. In 2D, and the experiments Refs. [35–57] are in 2D, we have qualitatively similar vertex corrections, but quantitatively the corrections are much weaker and a displacement of the Drude peak not conceivable yet, we just see a renormalization of the Drude peak.

Finally, when it comes to the maximum values of χ_{VERT} and σ_{VERT} and the height of the displaced Drude peak in the total optical conductivity, from Figs. 4(a) and 4(c) it is evident that they all increase as the phase transition is approached. Interestingly, in the 1D case we roughly have $\max_{\omega > 0} \sigma_{\text{VERT}}(\omega) \sim (T - T_c)^{-1}$, while in the 2D case $\max_{\omega > 0} \sigma_{\text{VERT}}(\omega) \sim \ln[(T - T_c)^{-1}]$ [note the logarithmic scale in Fig. 4(c)]. This scaling further supports our findings that the RPA π-ton vertex corrections are smaller in 2D than in 1D for the temperature ranges considered. Moreover, it also suggests that addressing the regime with potentially larger π-ton vertex corrections in 2D very close to the transition boundary is very challenging due to the required numerical accuracy.

D. Comments on the relation to previous results

The displaced Drude peak was not observed in the earlier 1D RPA treatments of the π-ton vertex corrections [32,33]. To understand the discrepancies between those previous and the present results, we here recalculate the bubble and the π-ton vertex contributions to the current-current correlation function on the imaginary axis for the parameter set S_{DMFT} and the temperature $T = 0.08$ following the approach of Ref. [32].

Motivated by the convergence challenges discussed in Sec. III B, in Fig. 5(b) we show the π-ton vertex contributions on the Matsubara axis for four different momentum grids. It is apparent that χ_{VERT} for the grid $N_k = 41$, which roughly equals the number of momentum points used previously in Refs. [32,33], differs quite significantly from the results for denser momentum grids. Not only is the magnitude of χ_{VERT} roughly four times smaller for the first few Matsubara frequencies but more importantly, the slope between zero and the first Matsubara frequency becomes positive in the latter cases. Those differences can be even more pronounced for temperatures closer to the transition boundary, such as those considered in Ref. [32].

In order to obtain the optical conductivity spectra on the real-frequency axis from the current-current correlation functions in Figs. 5(a)–5(c), we carry out an analytic continuation using the ana_cont package [62]. We analytically continue only χ_{BUB} and χ_{TOT}, while the π-ton vertex contributions are obtained as the difference $\sigma_{\text{VERT}} = \sigma_{\text{TOT}} - \sigma_{\text{BUB}}$. More details on the analytic continuation are given in Appendix C.

In Figs. 5(d)–5(f), we show the resulting optical conductivity spectra for an optimal set of analytic continuation
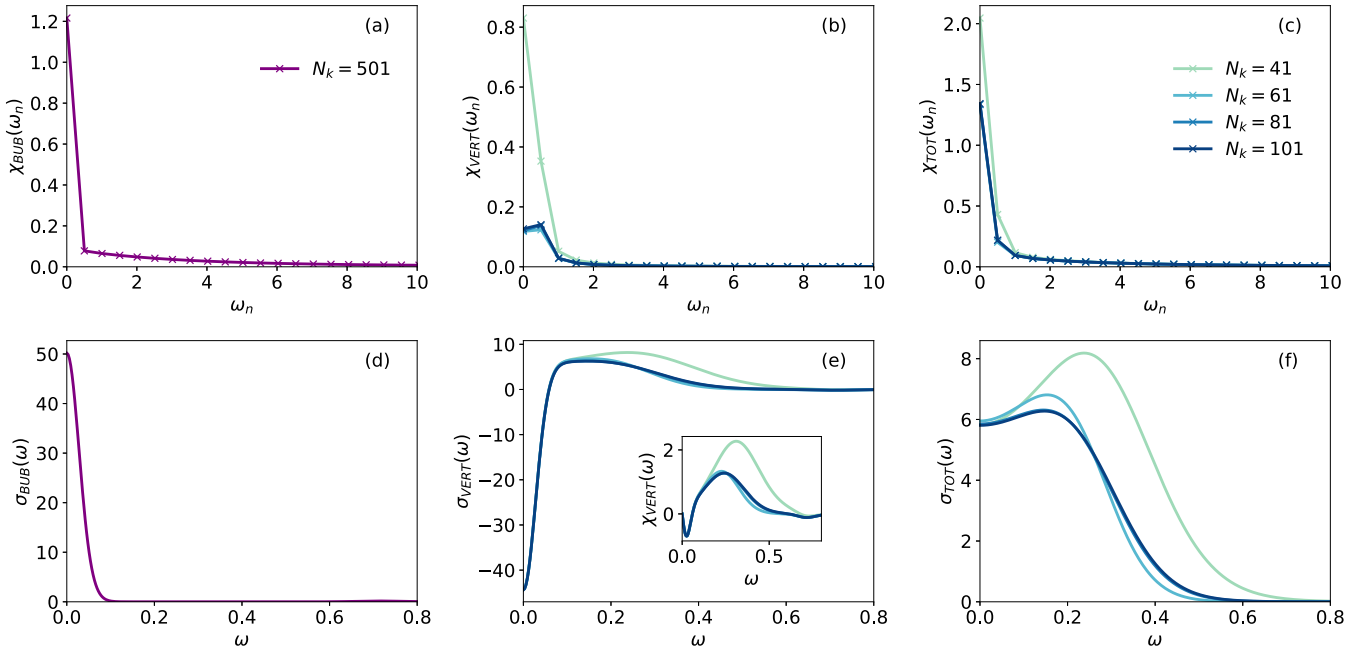
FIG. 5. [(a)–(c)] Bubble, RPA π-ton vertex, and total contribution to the current-current correlation function on the Matsubara axis calculated for the parameter set S_{DMFT} with $T = 0.08$ and several momentum grids N_k. [(d)–(f)] Corresponding optical conductivity spectra on the real-frequency axis. The inset of panel (e) further shows the current-current correlation function for real frequencies.

parameters. We conclude that the overall shape of the π-ton vertex corrections σ_{VERT} is quite robust to different analytic continuation parameters, that σ_{VERT} is converged for $N_k = 81$, and that it actually shows a similar qualitative behavior as the shape of the π-ton vertex corrections predicted in Secs. III A and III B. Namely, the π-ton vertex corrections, Fig. 5(e), tend to suppress the optical conductivity at low frequencies and enhance it at higher ones, producing together with the bubble contribution the displaced Drude peak, see Fig. 5(f).

The enhancement of the current-current correlation function by the π-ton vertex contributions for the case with $N_k = 41$, see inset of Fig. 5(e), is maximal around $\omega \approx 0.31$, while for low frequencies, $\omega < 0.06$, the π-ton vertex contributions are rather negative. For exactly the same parameters, the π-ton vertex contributions were calculated directly on the real-frequency axis in Ref. [33]. While a broad peak, similar to the one in the inset of Fig. 5(e), was reported around $\omega \approx 0.35$, the π-ton vertex contributions were reported to be positive all the way down to the zero frequency. We note, however, that in Ref. [33] a Fourier transformation with time window $\Delta t = 17$ was used, which implies a smearing of the low-frequency features, $\omega < (\Delta t)^{-1}$. This might explain why no negative vertex correction was observed at small frequencies.

As a last remark, we note that the results in Fig. 5 are obtained with DMFT Green's functions which, apart from the quasiparticle pole, contain the incoherent contribution corresponding to the Hubbard bands. Our results suggest that for relatively weak interactions the Hubbard bands play little to no role in shaping the qualitative behavior of the π-ton vertex corrections. In other words, the displaced Drude peak is obtained solely by considering vertex corrections of the low-energy quasiparticle excitations. It is not an additional

peak but as if the Drude peak itself was shifted away from $\omega = 0$.

IV. CONCLUSIONS

Our main finding is that π-ton vertex contributions result in a displaced Drude peak for, a true shift of the Drude peak to a maximum at a nonzero frequency. The presence of a displaced Drude peak in the 1D case is unambiguous with a linear scaling of the maximum of the displaced Drude peak with temperature (upon approaching the antiferromagnetic phase-transition temperature T_N). In the 2D case, we observe qualitatively the similar features for the π-ton vertex contributions, however, the logarithmic scaling in $T - T_N$ (instead of linear in 1D) makes unambiguous calculations in the regime with potentially larger π-ton vertex corrections practically impossible.

The displaced Drude peak was confirmed using the same two methods employed in earlier RPA studies of the π-ton contribution. That is the direct calculation for real frequencies and the analytic continuation of the Matsubara frequency calculation. As before, we employ a constant self-energy for the former and the IPT self-energy for the latter. Our paper is thus able to reconcile the apparent discrepancies between earlier results on π-ton vertex corrections in the weakly correlated Hubbard model. These reported a renormalization of the Drude peak [34], and an additional peak in the optical conductivity [32,33]. Let us emphasize the importance of a proper ν- and **k**-grid convergence. This is challenging to achieve close to the antiferromagnetic phase transition, where π-ton effects become more pronounced and lead to the displaced Drude peak.

Our work shows that besides localization physics [5–8,59–61], displaced Drude peaks should also be expected

in general close to antiferromagnetic and charge density wave transitions. Our work hence shows an additional route to the displaced Drude peak: π-ton vertex corrections due to strong antiferromagnetic and charge density wave fluctuations. The effect is expected to be larger in 1D than in 2D.

One remaining question is: How can we distinguish this π-ton physics in the transversal particle-hole channel from localization effects in the particle-particle channel or external bosons such as low-energy phonons? One strategy for unambiguously identifying π-tons in an experiment would be to look at the change of the displaced Drude peak when approaching, e.g., an antiferromagnetic phase transition. We predict that if it is a π-ton peak, the overall effect will be enhanced closer to the phase transition.

The data of this paper are available in the repository hosted by TU Wien [80].

APPENDIX A: DETAILS ON THE CALCULATION OF THE CURRENT-CURRENT CORRELATION FUNCTION

We briefly outline the main ideas and formulas behind the real-axis approach of Ref. [34] and the imaginary-axis approach of Ref. [32] for calculating the current-current correlation function and in particular the π-ton vertex contributions.

The current-current correlation function can be diagrammatically represented as a sum of the bubble and the vertex contribution

$$
\chi_{jj}^{\alpha\beta}(q) = -\frac{2}{\beta N} \sum_k \gamma_{\mathbf{k q}}^{\alpha} \gamma_{\mathbf{k}(-\mathbf{q})}^{\beta} G_{k+q} G_k
$$
$$
- \frac{2}{\beta^2 N^2} \sum_{kk'} \gamma_{\mathbf{k q}}^{\alpha} \gamma_{\mathbf{k}'(-\mathbf{q})}^{\beta} G_{k+q} G_k F_d^{kk'q} G_{k'+q} G_{k'}
$$
$$
= \chi_{\mathrm{BUB}}^{\alpha\beta}(q) + \chi_{\mathrm{VERT}}^{\alpha\beta}(q). \tag{A1}
$$

Here $q = (\mathbf{q}, i\omega_n)$ denotes the four-momentum, while $\alpha, \beta = x, y, \ldots$ denote the direction in space. We consider only the diagonal elements, $\alpha = \beta$, of the tensor $\chi_{jj}^{\alpha\beta}$, and since we are dealing with an isotropic system, we further consider only the $\alpha = \beta = x$ case and drop the indices α and β.

We are interested in the optical conductivity for which we need the dynamic long-wavelength limit of the current-current correlation function. Therefore, we keep the frequency finite and set $\mathbf{q} = 0$ in $\chi_{jj}(q)$. Light-fermion vertices are then given in the Peierls approximation [81] where $\gamma_{\mathbf{k}}^x = \frac{\partial \varepsilon_{\mathbf{k}}}{\partial k_x}$ corresponds to the electron velocity.

Within the real-axis approach of Ref. [34], it is assumed that the retarded/advanced self-energy, $\Sigma_{\mathbf{k}, \nu}^{R/A}$, is

known on the real frequency axis. In terms of the self-energy, the retarded/advanced Green's function is given by $G_{\mathbf{k}, \nu}^{R/A} = \frac{1}{\nu - \varepsilon_{\mathbf{k}} - \Sigma_{\mathbf{k}, \nu}^{R/A}}$, and the spectral function further as $A_{\mathbf{k}, \nu} = \mp \mathrm{Im} G_{\mathbf{k}, \nu}^{R/A} / \pi$. To translate the sums over Matsubara frequencies $i\nu_n$ and $i\nu'_n$ in Eq. (A1) to real frequency integrals over ν and ν', a fact that the fermionic Matsubara frequencies are located at the poles of the Fermi-Dirac distribution $n_F(z) = \frac{1}{e^{\beta z}+1}$ is used, together with the property of the Green's function $G_{\mathbf{k}, z}$ that it is analytic everywhere expect for the real axis [34]. After transforming all fermionic Matsubara sums into integrals over real frequencies, the analytical continuation of $\chi(i\omega_n)$ can be handled by a simple substitution $i\omega_n \to \omega + i\eta$. For the bubble contribution, this procedure yields [34]

$$
\chi_{\mathrm{BUB}}(\omega) = -\frac{2}{N} \sum_{\mathbf{k}} \gamma_{\mathbf{k}}^2 \int_{-\infty}^{+\infty} d\nu \, n_F(\nu) A_{\mathbf{k}, \nu} \big[G_{\mathbf{k}, \nu+\omega}^R + G_{\mathbf{k}, \nu-\omega}^A \big]. \tag{A2}
$$

For the evaluation of the vertex contribution, a similar procedure is used. It is additionally assumed that the vertex function depends on only one transfer momentum/frequency $F_d^{kk'q} \equiv F_d^{k-k}$, and that its complex structure is the same as that of a physical magnetic susceptibility, i.e., it is analytic in the whole complex plane except for the real axis where it has a branch cut. These assumptions are readily valid for the RPA π-ton and the Ornstein-Zernike vertex functions in Eqs. (3) and (5), respectively. Without going into any further details, here we just recall the final expressions for the vertex contribution to the current-current correlation function in Ref. [34]

$$
\chi_{\mathrm{VERT}}(\omega) = -\frac{2}{N^2} \sum_{\mathbf{kk'}} \gamma_{\mathbf{k}} \gamma_{\mathbf{k'}} \big[\zeta_1^{\mathbf{kk'}}(\omega) + \zeta_2^{\mathbf{kk'}}(\omega) + \zeta_3^{\mathbf{kk'}}(\omega) \big], \tag{A3}
$$

with

$$
\zeta_1^{\mathbf{kk'}}(\omega) = -\frac{1}{4\pi^2} \int_{-\infty}^{+\infty} \int_{-\infty}^{+\infty} d\nu \, d\nu' \, n_F(\nu) \, n_B(\nu')
$$
$$
\times \big[F_{\mathbf{k}-\mathbf{k'}, -\nu'}^R - F_{\mathbf{k}-\mathbf{k'}, -\nu'}^A \big]
$$
$$
\times \big[G_{\mathbf{k}, \nu}^R G_{\mathbf{k'}, \nu+\nu'}^R - G_{\mathbf{k}, \nu}^A G_{\mathbf{k'}, \nu+\nu'}^A \big]
$$
$$
\times \big[G_{\mathbf{k}, \nu+\omega}^R G_{\mathbf{k'}, \nu+\nu'+\omega}^R + G_{\mathbf{k}, \nu-\omega}^A G_{\mathbf{k'}, \nu+\nu'-\omega}^A \big], \tag{A4}
$$

$$
\zeta_2^{\mathbf{kk'}}(\omega) = \frac{i}{2\pi} \int_{-\infty}^{+\infty} \int_{-\infty}^{+\infty} d\nu \, d\nu' \, n_F(\nu) \, n_F(\nu') A_{\mathbf{k'}, \nu'}
$$
$$
\times \big[G_{\mathbf{k}, \nu}^R F_{\mathbf{k}-\mathbf{k'}, \nu-\nu'}^R - G_{\mathbf{k}, \nu}^A F_{\mathbf{k}-\mathbf{k'}, \nu-\nu'}^A \big]
$$
$$
\times \big[G_{\mathbf{k}, \nu+\omega}^R G_{\mathbf{k'}, \nu'+\omega}^R + G_{\mathbf{k}, \nu-\omega}^A G_{\mathbf{k'}, \nu'-\omega}^A \big], \tag{A5}
$$

and

$$
\zeta_3^{\mathbf{kk'}}(\omega) = \int_{-\infty}^{+\infty} \int_{-\infty}^{+\infty} d\nu \, d\nu' \, n_F(\nu) \, n_F(\nu') A_{\mathbf{k}, \nu} A_{\mathbf{k'}, \nu'}
$$
$$
\times \big[G_{\mathbf{k'}, \nu'+\omega}^R G_{\mathbf{k}, \nu-\omega}^A F_{\mathbf{k}-\mathbf{k'}, \nu-\nu'-\omega}^A
$$
$$
- G_{\mathbf{k'}, \nu'-\omega}^A G_{\mathbf{k}, \nu+\omega}^R F_{\mathbf{k}-\mathbf{k'}, \nu-\nu'+\omega}^R \big]. \tag{A6}
$$

Contrary, in the imaginary axis approach of Ref. [32], the DMFT self-energy $\Sigma(i\nu_n)$ is first obtained using the iterated perturbation theory on the imaginary axis. From $\Sigma(i\nu_n)$, the Green's function G_k, the Lindhard function $\chi_q^0 = $
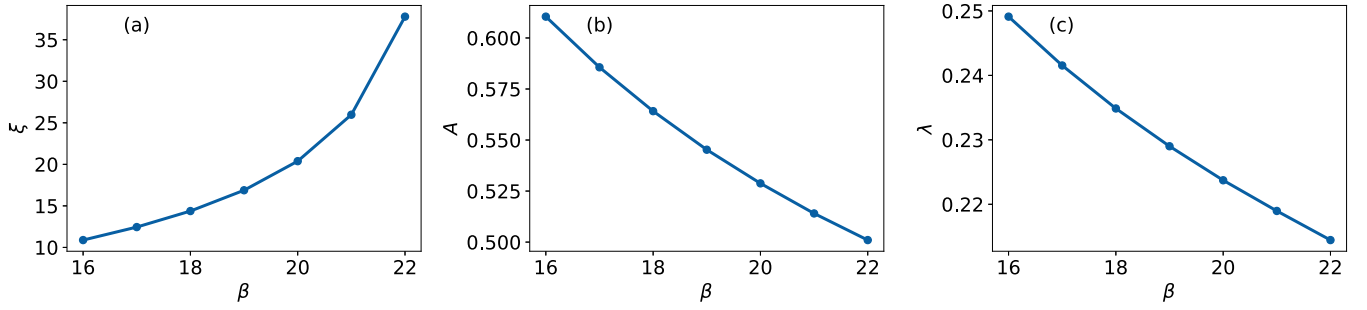
FIG. 6. Inverse temperature dependence of the Ornstein-Zernike parameters ξ, A, and λ extracted by fitting the Ornstein-Zernike form in Eq. (5) to the RPA π-ton vertex function in Eq. (3) for the parameter set S_{1D}.

$-\frac{1}{\beta}\sum_k G_k G_{k+q}$, and the RPA π-ton vertex function $F^{RPA}_{\overline{ph},k-k'}$ are further obtained. Finally, the current-current correlation function on the imaginary axis is calculated by explicitly performing the sums over Matsubara frequencies in Eq. (A1), with $F^{RPA}_{\overline{ph},k-k'}$ entering the corresponding expressions.

APPENDIX B: FIT OF THE ORNSTEIN-ZERNIKE FORM TO THE RPA π-TON VERTEX FUNCTION

We extract the Ornstein-Zernike parameters A, λ, and ξ in Eq. (5) from the RPA π-ton vertex function in Eq. (3) in three steps. First, we calculate the real part of the static RPA π-ton vertex function around the wave vector $q = \pi$, as well as the low-frequency limit of the RPA π-ton vertex function at $q = \pi$, using dense momentum and frequency grids, with $N_k = 1000$ and $N_\nu = 7993$ points, respectively. Then in the second step, we consider the inverse of the static Ornstein-Zernike function around $q = \pi$,

$$\left[F^{OZ}_{q\approx\pi,\omega}\right]^{-1} \approx \frac{1}{A}q^2 + \frac{\xi^{-2}}{A}, \qquad (B1)$$

and fit the second-order polynomial, $aq^2 + c$, to the calculated static RPA π-ton vertex function around $q \approx \pi$. The inverse of the coefficient a gives us the parameter $A = a^{-1}$, while the correlation length is obtained as $\xi = \sqrt{a/c}$.

In the last (third) step we fit the frequency dependence. To this end, we consider the inverse of the real part of the Ornstein-Zernike function at $q = \pi$,

$$\left[F^{OZ}_{q=\pi,\omega}\right]^{-1} \approx \frac{\lambda^2}{A\xi^{-2}}\omega^2 + \frac{A}{\xi^{-4}}, \qquad (B2)$$

and again fit a second-order polynomial, $a'\omega^2 + c'$, now to the low frequency part of the RPA π-ton vertex function at $q = \pi$. We use the coefficient a' together with the previously extracted A and ξ to finally obtain $\lambda = \sqrt{a'A}/\xi$.

Following the above procedure, we extract from the RPA π-ton vertex function the Ornstein-Zernike parameters for the parameter set S_{1D} and inverse temperatures $\beta = 16 - 22$. The corresponding inverse temperature dependence of parameters ξ, A, and λ are shown in Fig. 6, while in Fig. 7, we show the RPA π-ton vertex function together with its approximate Ornstein-Zernike form for the inverse temperature $\beta = 17$.

APPENDIX C: DETAILS ON THE ANALYTIC CONTINUATION OF THE CURRENT-CURRENT CORRELATION FUNCTION

The analytic continuation of the current-current correlation functions $\chi_{jj}(i\omega_n)$ in Figs. 5(a)–5(c) is carried out by means of the maximum entropy method as implemented within the `ana_cont` package [62]. The solver of `ana_cont` directly returns $\sigma(\omega)$, which is related to $\chi_{jj}(i\omega_n)$ with a kernel $K_b(\omega_n, \omega) = \frac{\omega^2}{\omega_n^2 + \omega^2}$ as $\chi_{jj}(i\omega_n) = \int_0^\infty d\omega K_b(\omega_n, \omega)\sigma(\omega)$. We analytically continue only the bubble and the total contributions, while the π-ton vertex contributions to the optical conductivity are obtained as the difference, $\sigma_{VERT} = \sigma_{TOT} - \sigma_{BUB}$. As input to our analytic continuation problem, we use the values $\chi_{jj}(i\omega_n)$ for the first 30 positive Matsubara frequencies, including the zero frequency, normalized with respect to the value of χ_{jj} at zero Matsubara frequency. Additionally, we set the amplitude of error to 5×10^5 and 5×10^3
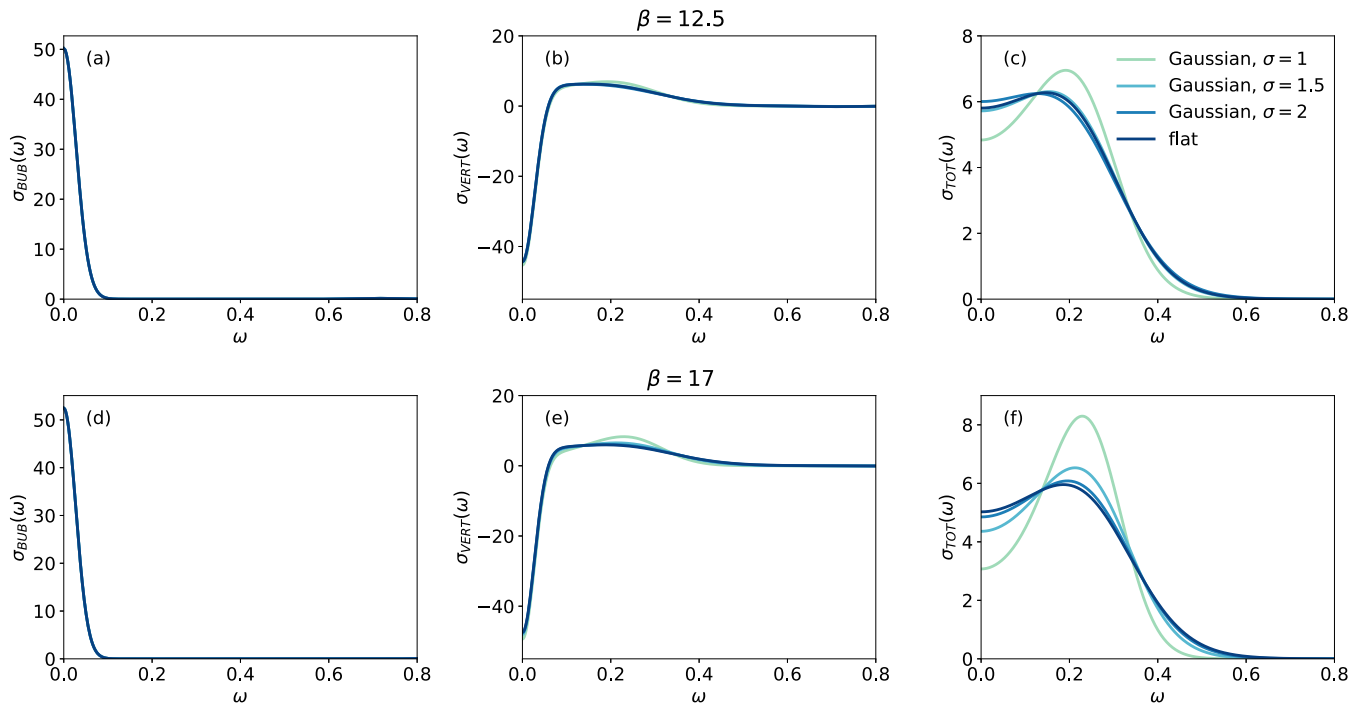
$\beta = 17$

FIG. 7. Real part of the Ornstein-Zernike vertex function (green dashed line) fitted to the RPA π-ton vertex function (blue solid line) for the parameter set S_{1D} and the inverse temperature $\beta = 17$, as a function of (a) q for a fixed $\omega = 0$ and (b) ω for a fixed $q = \pi$.

FIG. 8. Bubble [(a) and (d)], π-ton vertex [(b) and (e)], and total contribution [(c) and (f)] to the optical conductivity obtained with the analytic continuation using the chi2kink method and several different default models, for the parameter set S_{DMFT}, the momentum grid $N_k = 101$, and two inverse temperatures $\beta = 12.5$ [(a)–(c)] and $\beta = 17$ [(d)–(f)].

for the bubble and the total contribution, respectively. The corresponding real frequency spectra are computed on the grid $[0, \lfloor \frac{2\pi}{\beta} \times 30 \rfloor]$ with 5000 points.

The method for determining the hyperparameter α and the model for the prior probability of the spectrum have a significant influence on the behavior of the resulting spectra; see Ref. [62] for further information on these parameters, the chi2kink method and Gaussian broadening. For example, in Fig. 8 we show the spectra for the parameter set S_{DMFT}, calculated with $N_k = 101$ momentum points, and two inverse temperatures $\beta = 12$ and $\beta = 17$, obtained with the chi2kink method and employing several models. In particular, we compare the spectra obtained with the flat model and Gaussian functions with various widths σ. Although the

displaced Drude peak is clearly visible in all cases considered, choosing a thinner Gaussian leads to a more pronounced displaced Drude peak behavior. This is particularly evident in the case with $\sigma = 1$, where the π-ton vertex corrections may appear to tend to peak around $\omega \sim 0.2$ as the temperature is lowered, see Figs. 8(b) and 8(e).

In the main text, we present the results obtained with the chi2kink method and the flat model, in order to avoid any bias towards an extremely sharp displaced Drude peak in the total optical conductivity. Although, as expected, the displaced Drude peak is more pronounced for the inverse temperature $\beta = 17$, in the main text we present the case with $\beta = 12.5$ to enable a direct comparison of our new results with those obtained in Ref. [33].

[1] P. Drude, Zur elektronentheorie der metalle, Ann. Phys. **306**, 566 (1900).

[2] P. Drude, Zur elektronentheorie der metalle; II. Teil. Galvanomagnetische und thermomagnetische effecte, Ann. Phys. **308**, 369 (1900).

[3] J. Frenkel, On the transformation of light into heat in solids. I, Phys. Rev. **37**, 17 (1931).

[4] G. H. Wannier, The structure of electronic excitation levels in insulating crystals, Phys. Rev. **52**, 191 (1937).

[5] E. Abrahams, P. W. Anderson, D. C. Licciardello, and T. V. Ramakrishnan, Scaling theory of localization: Absence of quantum diffusion in two dimensions, Phys. Rev. Lett. **42**, 673 (1979).

[6] L. P. Gor'kov, A. I. Larkin, and D. E. Khmel'Nitskii, Particle conductivity in a two-dimensional random potential, in

30 Years of the Landau Institute - Selected Papers, edited by I. M. Khalatnikov *et al.* (World Scientific, Singapore, 1996), pp. 157–161.

[7] W. Götze, P. Prelovšek, and P. Wölfle, Localization of particles in a two-dimensional random potential, Solid State Commun. **30**, 369 (1979).

[8] B. L. Altshuler, D. Khmel'nitzkii, A. I. Larkin, and P. A. Lee, Magnetoresistance and Hall effect in a disordered two-dimensional electron gas, Phys. Rev. B **22**, 5142 (1980).

[9] D. G. Clarke, Particle-hole bound states in Mott-Hubbard insulators, Phys. Rev. B **48**, 7520 (1993).

[10] H. Maebashi and H. Fukuyama, Electrical conductivity of interacting fermions. I. General formulation, J. Phys. Soc. Jpn. **66**, 3577 (1997).

[11] F. H. L. Essler, F. Gebhard, and E. Jeckelmann, Excitons in one-dimensional Mott insulators, Phys. Rev. B **64**, 125119 (2001).

[12] P. Wróbel and R. Eder, Excitons in Mott insulators, Phys. Rev. B **66**, 035111 (2002).

[13] E. Jeckelmann, Optical excitations in a one-dimensional Mott insulator, Phys. Rev. B **67**, 075106 (2003).

[14] H. Kontani, Optical conductivity and Hall coefficient in high-Tc superconductors: Significant role of current vertex corrections, J. Phys. Soc. Jpn. **75**, 013703 (2006).

[15] N. Lin, E. Gull, and A. J. Millis, Optical conductivity from cluster dynamical mean-field theory: Formalism and application to high-temperature superconductors, Phys. Rev. B **80**, 161105(R) (2009).

[16] D. Bergeron, V. Hankevych, B. Kyung, and A.-M. S. Tremblay, Optical and dc conductivity of the two-dimensional Hubbard model in the pseudogap regime and across the antiferromagnetic quantum critical point including vertex corrections, Phys. Rev. B **84**, 085128 (2011).

[17] A. V. Chubukov, D. L. Maslov, and V. I. Yudson, Optical conductivity of a two-dimensional metal at the onset of spin-density-wave order, Phys. Rev. B **89**, 155126 (2014).

[18] J. Kokalj, Bad-metallic behavior of doped Mott insulators, Phys. Rev. B **95**, 041110(R) (2017).

[19] D. L. Maslov and A. V. Chubukov, Optical response of correlated electron systems, Rep. Prog. Phys. **80**, 026503 (2017).

[20] J. Vučičević, J. Kokalj, R. Žitko, N. Wentzell, D. Tanasković, and J. Mravlje, Conductivity in the square lattice Hubbard model at high temperatures: Importance of vertex corrections, Phys. Rev. Lett. **123**, 036601 (2019).

[21] E. W. Huang, R. Sheppard, B. Moritz, and T. P. Devereaux, Strange metallicity in the doped Hubbard model, Science **366**, 987 (2019).

[22] P. Pudleiner, P. Thunström, A. Valli, A. Kauch, G. Li, and K. Held, Parquet approximation for molecules: Spectrum and optical conductivity of the Pariser-Parr-Pople model, Phys. Rev. B **99**, 125111 (2019).

[23] A. Kauch, P. Pudleiner, K. Astleithner, P. Thunström, T. Ribic, and K. Held, Generic optical excitations of correlated systems: π-tons, Phys. Rev. Lett. **124**, 047401 (2020).

[24] K. Astleithner, A. Kauch, T. Ribic, and K. Held, Parquet dual fermion approach for the Falicov-Kimball model, Phys. Rev. B **101**, 165101 (2020).

[25] N. E. Bickers, Self-consistent many-body theory for condensed matter systems, in *Theoretical Methods for Strongly Correlated Electrons*, edited by D. Sénéchal, A.-M. Tremblay, and C. Bourbonnais (Springer New York, New York, 2004), pp. 237–296.

[26] G. Li, N. Wentzell, P. Pudleiner, P. Thunström, and K. Held, Efficient implementation of the parquet equations: Role of the reducible vertex function and its kernel approximation, Phys. Rev. B **93**, 165103 (2016).

[27] G. Li, A. Kauch, P. Pudleiner, and K. Held, The victory project v1.0: An efficient parquet equations solver, Comput. Phys. Commun. **241**, 146 (2019).

[28] H. Kusunose, Influence of spatial correlations in strongly correlated electron systems: Extension to dynamical mean field approximation, J. Phys. Soc. Jpn. **75**, 054713 (2006).

[29] A. Toschi, A. A. Katanin, and K. Held, Dynamical vertex approximation: A step beyond dynamical mean-field theory, Phys. Rev. B **75**, 045118 (2007).

[30] A. A. Katanin, A. Toschi, and K. Held, Comparing pertinent effects of antiferromagnetic fluctuations in the two- and three-dimensional Hubbard model, Phys. Rev. B **80**, 075104 (2009).

[31] L. M. Falicov and J. C. Kimball, Simple model for semiconductor-metal transitions: SmB_6 and transition-metal oxides, Phys. Rev. Lett. **22**, 997 (1969).

[32] O. Simard, S. Takayoshi, and P. Werner, Diagrammatic study of optical excitations in correlated systems, Phys. Rev. B **103**, 104415 (2021).

[33] O. Simard, M. Eckstein, and P. Werner, Nonequilibrium evolution of the optical conductivity of the weakly interacting Hubbard model: Drude response and π-ton type vertex corrections, Phys. Rev. B **104**, 245127 (2021).

[34] P. Worm, C. Watzenböck, M. Pickem, A. Kauch, and K. Held, Broadening and sharpening of the Drude peak through antiferromagnetic fluctuations, Phys. Rev. B **104**, 115153 (2021).

[35] M. J. Rozenberg, G. Kotliar, H. Kajueter, G. A. Thomas, D. H. Rapkine, J. M. Honig, and P. Metcalf, Optical conductivity in Mott-Hubbard systems, Phys. Rev. Lett. **75**, 105 (1995).

[36] A. V. Puchkov, T. Timusk, S. Doyle, and A. M. Hermann, ab-plane optical properties of $Tl_2Ba_2CuO_{6+\delta}$, Phys. Rev. B **51**, 3312 (1995).

[37] A. A. Tsvetkov, J. Schützmann, J. I. Gorina, G. A. Kaljushnaia, and D. van der Marel, In-plane optical response of $Bi_2Sr_2CuO_6$, Phys. Rev. B **55**, 14152 (1997).

[38] N. L. Wang, S. Tajima, A. I. Rykov, and K. Tomimoto, Zn-substitution effects on the optical conductivity in $YBa_2Cu_3O_{7-\delta}$ crystals: Strong pair breaking and reduction of in-plane anisotropy, Phys. Rev. B **57**, R11081 (1998).

[39] T. Osafune, N. Motoyama, H. Eisaki, S. Uchida, and S. Tajima, Pseudogap and collective mode in the optical conductivity spectra of hole-doped ladders in $Sr_{14-x}Ca_xCu_{24}O_{41}$, Phys. Rev. Lett. **82**, 1313 (1999).

[40] K. Takenaka, Y. Sawaki, and S. Sugai, Incoherent-to-coherent crossover of optical spectra in $La_{0.825}Sr_{0.175}MnO_3$: Temperature-dependent reflectivity spectra measured on cleaved surfaces, Phys. Rev. B **60**, 13011 (1999).

[41] S. Lupi, P. Calvani, M. Capizzi, and P. Roy, Evidence of two species of carriers from the far-infrared reflectivity of $Bi_2Sr_2CuO_6$, Phys. Rev. B **62**, 12418 (2000).

[42] P. Kostic, Y. Okada, N. C. Collins, Z. Schlesinger, J. W. Reiner, L. Klein, A. Kapitulnik, T. H. Geballe, and M. R. Beasley, Non-Fermi-liquid behavior of $SrRuO_3$: Evidence from infrared conductivity, Phys. Rev. Lett. **81**, 2498 (1998).

[43] Y. S. Lee, J. Yu, J. S. Lee, T. W. Noh, T.-H. Gimm, H.-Y. Choi, and C. B. Eom, Non-Fermi liquid behavior and scaling of the low-frequency suppression in the optical conductivity spectra of $CaRuO_3$, Phys. Rev. B **66**, 041104(R) (2002).

[44] K. Takenaka, R. Shiozaki, and S. Sugai, Charge dynamics of a double-exchange ferromagnet $La_{1-x}Sr_xMnO_3$, Phys. Rev. B **65**, 184436 (2002).

[45] A. F. Santander-Syro, R. P. S. M. Lobo, N. Bontemps, Z. Konstantinovic, Z. Z. Li, and H. Raffy, Absence of a loss of in-plane infrared spectral weight in the pseudogap regime of $Bi_2Sr_2CaCu_2O_{8+\delta}$, Phys. Rev. Lett. **88**, 097005 (2002).

[46] K. Takenaka, J. Nohara, R. Shiozaki, and S. Sugai, Incoherent charge dynamics of $La_{2-x}Sr_xCuO_4$: Dynamical localization and resistivity saturation, Phys. Rev. B **68**, 134501 (2003).

[47] N. L. Wang, P. Zheng, T. Feng, G. D. Gu, C. C. Homes, J. M. Tranquada, B. D. Gaulin, and T. Timusk, Infrared properties of $La_{2-x}(Ca, Sr)_x CaCu_2 O_{6+\delta}$ single crystals, Phys. Rev. B **67**, 134526 (2003).

[48] N. E. Hussey, II, K. Takenaka, and H. Takagi, Universality of the Mott–Ioffe–Regel limit in metals, Philos. Mag. **84**, 2847 (2004).

[49] N. L. Wang, P. Zheng, D. Wu, Y. C. Ma, T. Xiang, R. Y. Jin, and D. Mandrus, Infrared probe of the electronic structure and charge dynamics of $Na_{0.7}CoO_2$, Phys. Rev. Lett. **93**, 237007 (2004).

[50] K. Takenaka, M. Tamura, N. Tajima, H. Takagi, J. Nohara, and S. Sugai, Collapse of coherent quasiparticle states in $\theta-(BEDT-TTF)_2 I_3$ observed by optical spectroscopy, Phys. Rev. Lett. **95**, 227801 (2005).

[51] P. E. Jönsson, K. Takenaka, S. Niitaka, T. Sasagawa, S. Sugai, and H. Takagi, Correlation-driven heavy-fermion formation in $LiV_2 O_4$, Phys. Rev. Lett. **99**, 167402 (2007).

[52] S. Kaiser, M. Dressel, Y. Sun, A. Greco, J. A. Schlueter, G. L. Gard, and N. Drichko, Bandwidth tuning triggers interplay of charge order and superconductivity in two-dimensional organic materials, Phys. Rev. Lett. **105**, 206402 (2010).

[53] R. Jaramillo, S. D. Ha, D. M. Silevitch, and S. Ramanathan, Origins of bad-metal conductivity and the insulator–metal transition in the rare-earth nickelates, Nat. Phys. **10**, 304 (2014).

[54] A. Biswas, O. Iakutkina, Q. Wang, H. C. Lei, M. Dressel, and E. Uykur, Spin-reorientation-induced band gap in $Fe_3 Sn_2$: Optical signatures of Weyl nodes, Phys. Rev. Lett. **125**, 076403 (2020).

[55] A. Pustogow, Y. Saito, A. Löhle, M. Sanz Alonso, A. Kawamoto, V. Dobrosavljević, M. Dressel, and S. Fratini, Rise and fall of Landau's quasiparticles while approaching the Mott transition, Nat. Commun. **12**, 1571 (2021).

[56] E. Uykur, B. R. Ortiz, O. Iakutkina, M. Wenzel, S. D. Wilson, M. Dressel, and A. A. Tsirlin, Low-energy optical properties of the nonmagnetic kagome metal $CsV_3 Sb_5$, Phys. Rev. B **104**, 045130 (2021).

[57] E. Uykur, B. R. Ortiz, S. D. Wilson, M. Dressel, and A. A. Tsirlin, Optical detection of the density-wave instability in the kagome metal $KV_3 Sb_5$, npj Quantum Mater. **7**, 16 (2022).

[58] L. V. Delacrétaz, B. Goutéraux, S. A. Hartnoll, and A. Karlsson, Bad metals from fluctuating density waves, SciPost Phys. **3**, 025 (2017).

[59] S. Fratini and S. Ciuchi, Displaced Drude peak and bad metal from the interaction with slow fluctuations, SciPost Phys. **11**, 039 (2021).

[60] H. Rammal, A. Ralko, S. Ciuchi, and S. Fratini, Transient localization from the interaction with quantum bosons, Phys. Rev. Lett. **132**, 266502 (2024).

[61] S. Fratini, K. Driscoll, S. Ciuchi, and A. Ralko, A quantum theory of the nearly frozen charge glass, SciPost Phys. **14**, 124 (2023).

[62] J. Kaufmann and K. Held, ana_cont: Python package for analytic continuation, Comput. Phys. Commun. **282**, 108519 (2023).

[63] A. Georges, G. Kotliar, W. Krauth, and M. J. Rozenberg, Dynamical mean-field theory of strongly correlated fermion systems and the limit of infinite dimensions, Rev. Mod. Phys. **68**, 13 (1996).

[64] H. Kajueter and G. Kotliar, New iterative perturbation scheme for lattice models with arbitrary filling, Phys. Rev. Lett. **77**, 131 (1996).

[65] P. Coleman, *Introduction to Many-Body Physics* (Cambridge University Press, Cambridge, UK, 2015).

[66] G. Rohringer, H. Hafermann, A. Toschi, A. A. Katanin, A. E. Antipov, M. I. Katsnelson, A. I. Lichtenstein, A. N. Rubtsov, and K. Held, Diagrammatic routes to nonlocal correlations beyond dynamical mean field theory, Rev. Mod. Phys. **90**, 025003 (2018).

[67] A. Khurana, Electrical conductivity in the infinite-dimensional Hubbard model, Phys. Rev. Lett. **64**, 1990 (1990).

[68] A. Mu, Z. Sun, and A. J. Millis, Optical conductivity of the two-dimensional Hubbard model: Vertex corrections, emergent Galilean invariance, and the accuracy of the single-site dynamical mean field approximation, Phys. Rev. B **106**, 085142 (2022).

[69] N. D. Mermin and H. Wagner, Absence of ferromagnetism or antiferromagnetism in one- or two-dimensional isotropic Heisenberg models, Phys. Rev. Lett. **17**, 1133 (1966).

[70] J. A. Hertz, Quantum critical phenomena, Phys. Rev. B **14**, 1165 (1976).

[71] A. J. Millis, H. Monien, and D. Pines, Phenomenological model of nuclear relaxation in the normal state of $YBa_2 Cu_3 O_7$, Phys. Rev. B **42**, 167 (1990).

[72] H. v. Löhneysen, A. Rosch, M. Vojta, and P. Wölfle, Fermi-liquid instabilities at magnetic quantum phase transitions, Rev. Mod. Phys. **79**, 1015 (2007).

[73] T. Schäfer, N. Wentzell, F. Šimkovic, Y.-Y. He, C. Hille, M. Klett, C. J. Eckhardt, B. Arzhang, V. Harkov, F.-M. Le Régent, A. Kirsch, Y. Wang, A. J. Kim, E. Kozik, E. A. Stepanov, A. Kauch, S. Andergassen, P. Hansmann, D. Rohe, Y. M. Vilk *et al.*, Tracking the footprints of spin fluctuations: A multi-method, multimessenger study of the two-dimensional Hubbard model, Phys. Rev. X **11**, 011058 (2021).

[74] S. G. Johnson, Multi-dimensional adaptive integration in C: The Cubature package, https://github.com/stevengj/cubature (2005).

[75] F. Krien, Conserving dynamical mean-field approaches to strongly correlated systems, Ph.D. thesis, University of Hamburg, 2018.

[76] H. Hafermann, E. G. C. P. van Loon, M. I. Katsnelson, A. I. Lichtenstein, and O. Parcollet, Collective charge excitations of strongly correlated electrons, vertex corrections, and gauge invariance, Phys. Rev. B **90**, 235105 (2014).

[77] E. Jeckelmann, F. Gebhard, and F. H. L. Essler, Optical conductivity of the half-filled Hubbard chain, Phys. Rev. Lett. **85**, 3910 (2000).

[78] C. Karrasch, D. M. Kennes, and J. E. Moore, Transport properties of the one-dimensional Hubbard model at finite temperature, Phys. Rev. B **90**, 155104 (2014).

[79] A. C. Tiegel, T. Veness, P. E. Dargel, A. Honecker, T. Pruschke, I. P. McCulloch, and F. H. L. Essler, Optical conductivity of the Hubbard chain away from half filling, Phys. Rev. B **93**, 125108 (2016).

[80] https://doi.org/10.48436/3v9ge-25734.

[81] R. Peierls, Zur theorie des diamagnetismus von leitungselektronen, Z. Phys. **80**, 763 (1933).